Josephson vortices and persistent current in a double-ring supersolid system

M. Schubert [1,*] K. Mukherjee [1,†] T. Pfau [2] and S. M. Reimann [1]
[1]Mathematical Physics and NanoLund, Lund University, Box 118, 22100 Lund, Sweden
[2]Physikalisches Institut and Center for Integrated Quantum Science and Technology, Universität Stuttgart, Pfaffenwaldring 57, 70569 Stuttgart, Germany

(Received 14 March 2025; accepted 23 June 2025; published 1 August 2025)

We theoretically investigate the properties of ultracold dipolar atoms in radially coupled, concentric annular traps created by a potential barrier. The nonrotating ground-state phases are investigated across the superfluid-supersolid phase transition, revealing a particle imbalance between the two rings and a preferential density modulation in the outer ring in the absence of rotation. Near the phase transition on the superfluid side, applying rotation can induce density modulations in either ring, depending on the angular momentum and barrier strength. For low angular momentum, such rotation-induced density modulation forms in the outer ring, while for high angular momentum and weak barriers, it emerges in the inner ring. Rotation can lead to persistent currents and the nucleation of a vortex residing either at the center (central vortex) or at the ring junction (Josephson vortex). Josephson vortices can also form at the junctions of the localized density sites induced by rotation in the inner ring, a behavior that is unique to our system. By switching off the trap and allowing the system to expand, distinct interference patterns emerge, which can be analyzed to identify and distinguish between various vortex configurations, and thus can be observed in current state-of-the-art experiments.

DOI: 10.1103/tl7c-v5bs

I. INTRODUCTION

Superfluidity is well known to be closely related to the phenomenon of Bose-Einstein condensation (BEC) [1–3] and manifests through the existence of vortices and persistent currents (see the review [4]). In analogy to superconducting rings [5,6], multiply connected atomic condensates in toroidal traps may exhibit metastable flow [7–15] (see also the recent review [16]). Likewise, the Josephson effect (originally discovered in superconducting systems [17]) may govern the tunneling between purely superfluid (SF) states that are weakly linked by a junction formed by an external potential. For singly connected systems, the atomic analog of the Josephson effect has been intensively studied, see, e.g., Refs. [18–27]. Particularly interesting, however, is the combination of the Josephson effect and persistent flow that can be achieved by trapping a BEC in a double (or multiple) ring geometry, arranged coaxially or coplanarly [28–39]. The coupling between the rings across an azimuthally symmetric barrier may then lead to an intriguing interplay between Josephson tunneling and persistent currents (PCs) in the system. A distinctive feature of such multiring potentials is their ability to support either identical or distinctly quantized flows across the junctions, with some or all of the rings carrying quantized angular momentum. The phase difference between the rings leads to the formation of vortices at the Josephson barriers, commonly referred to as Josephson vortices (JVs). They have been observed in superconductors [40] and polariton superfluids [41], and are also well studied in BECs of alkali atoms [25,29,37,38,42–45].

Dipolar BECs (as reviewed in [46–49]) add another interesting twist to the physics of JVs and PCs, due to the long-range interaction. After first experiments with chromium [50,51], lanthanides with larger magnetic dipole moments [52–55] became of interest, where similarly to a classical Rosensweig transition, regular arrays of droplets may form [56,57]. Under certain conditions, these droplets may phase-coherently overlap, and a periodic solid-like structure may emerge while the coherent superfluid properties are partly maintained [58–61]. Such a "supersolid" (SS) state of matter was predicted early on [1] for helium but remained elusive [62]. Unequivocal evidence for its existence, however, only came more recently from the above experiments with ultracold dysprosium [58–61] and erbium [60]. Subsequent studies analyzed the excitation spectra [63,64] associated with the SF-SS transition and provided deeper insights into various dynamical phenomena [65]. Vortices as indicators of superfluidity in the SS state were also studied [66–70]. Interestingly, already long before the realization of SSs, it was suggested that an SF of dipolar atoms polarized perpendicular to the symmetry axis of a toroidal trap will form a self-induced Josephson junction, splitting the SF into two halves on either side of the ring [71]. More recently, the SS state has been interpreted as an array of such junctions [72–75], albeit here as a consequence of the SS density modulation. A connection could be drawn between the superfluid fraction as a measure

*Contact author: malte.schubert@fysik.lu.se
†Contact author: koushik.mukherjee@fysik.lu.se

Published by the American Physical Society under the terms of the Creative Commons Attribution 4.0 International license. Further distribution of this work must maintain attribution to the author(s) and the published article's title, journal citation, and DOI. Funded by Bibsam.

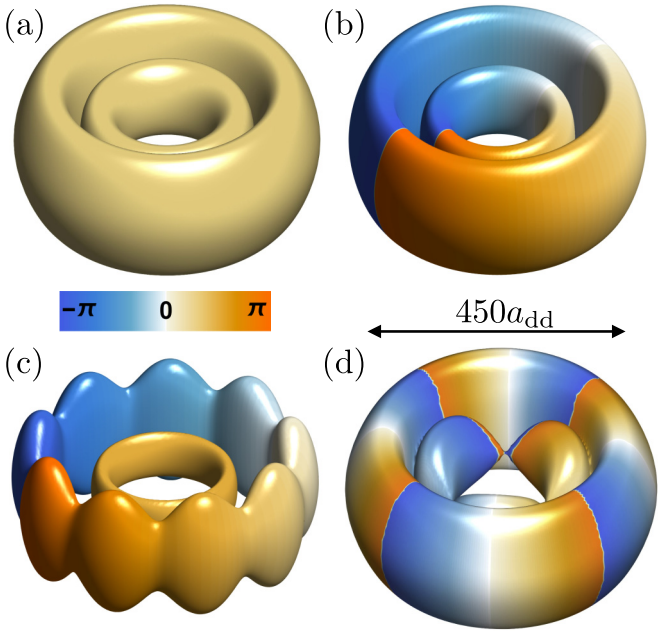


FIG. 1. Density isosurfaces in ground states showcasing SF states [upper panel, (a), (b)] and SS states [lower panel, (c), (d)]. The color of the isosurface at each position represents the value of the phase associated with the wave function. (a) Nonrotating ground state for $\epsilon_{dd} = 1.95$ and $V_B = 10^4 a_{dd}^2$. (b) Rotating ground state with a CV obtained for the same parameters as in (a), but for a trap rotation with $\Omega = 0.04\omega$. (c) Rotating ground state with a JV_1 for $\epsilon_{dd} = 2.05$, $V_B = 6 \times 10^4 a_{dd}^2$ and $\Omega = 0.04\omega$. (d) Rotating ground state with three JV_2s. The parameters here are the same as in (a), but with $\Omega = 0.12\omega$. The isosurfaces are plotted at values of 10% of the maximum density for (a)–(c) and at 38% for (d).

of the density modulation in the SS and the Josephson effect [72]. For a dipolar SS in a toroidal trap, earlier studied in [76–78] and yet to be realized experimentally, the absence of inhomogeneities typical of cigar-shaped traps leads to a collective excitation spectrum where first sound, second sound, and Higgs modes can decouple [79]. When persistent current exists, the angular momentum per particle (in the SS being less than unity in units of $\hbar$) is determined by the superfluid fraction [76–78].

In this work, motivated by the advantages of the toroidal confinement and the existence of novel phases in dipolar BECs, we investigate dipolar BECs confined in coplanar double rings sharing a common center (as displayed by the density isosurfaces in Fig. 1). Pertinent questions are how the spontaneous density modulation of the SS state evolves in a double-ring as the relative dipolar interaction strength increases, how the persistent current develops, and how topological defects emerge in the presence of rotation.The system remains in a pure SF state when both rings exhibit azimuthally uniform density profiles, as shown in Figs. 1(a) and 1(b). If a density modulation occurs in one or both rings, The system may also form an SS state [Figs. 1(c) and 1(d)], with a density modulation in one or both of the rings. We note that such an SS system contains two types of junctions: (1) one between the rings, produced artificially by the azimuthally symmetric barrier between the rings, and (2) those formed by the atoms that take part in the superfluid flow of the SS.

The long-range dipolar interaction creates a population difference between the rings, and the supersolid density modulation preferentially appears in the outer ring in the absence of rotation. Near the SF-SS phase transition, a system that initially is in an SF state can form a density modulation when forced to acquire angular momentum through rotation. This may happen either in the outer or inner ring, depending on the system's angular momentum and the barrier strength. For relatively small angular momentum, it is the outer ring that contributes to the formation of the SS, regardless of the barrier strength. For large angular momentum, if the barrier is weak, rotation can facilitate the formation of an SS in the inner ring.

When a critical rotation frequency is exceeded, topological defects such as vortices are nucleated as a consequence of the superfluid properties of the system, and also, persistent currents may occur. A nonzero density along the azimuthal barrier, i.e., in between the two rings, significantly affects the pathway of vortex nucleation. We in the following refer to vortices that are located at the junction barrier between the rings as JV_1 [Fig. 1(c)]. In this case, metastable persistent current exists only in the outer ring, as we observe only for the isolated rings. The entire system can exhibit a persistent current when a vortex is located at the center, referred to as a central vortex (CV), which occurs when a density bridge exists between the rings due to a weaker barrier [Fig. 1(b)]. In this latter configuration, sufficiently high rotation can induce the formation of periodic density modulation in the inner ring, with vortices located at the junctions between the density sites [Fig. 1(d)]. These JVs are unique to the double-ring dipolar system, where the system's tendency to form spontaneous density modulation makes their existence possible. We refer to them as JV_2. Notably, these structures can be observed in experiments through the interference of different parts of the condensate, producing distinct patterns when the trap is switched off.

The remainder of this paper is organized as follows: We introduce our setup and theoretical framework in Sec. II. Our results are discussed in Sec. III. Specifically, we first examine the static ground-state structures that develop in the double-ring system in Sec. III A. The rotational dynamics of the system are then analyzed in Sec. III B under two distinct configurations: one where the rings remain separated [Sec. III B 1] and another where they are connected [Sec. III B 2]. A phase diagram explaining the existence of JVs and CVs is presented in Sec. III B 2. We discuss how interferometric techniques can be used to distinguish between these states in Sec. III B 3. After conclusive remarks and an outlook in Sec. IV, Appendixes A and B provide some additional details of the numerical simulations and analytical expressions, respectively, performed in this work.

II. MODEL AND METHODS

The confinement setup can be realized using a toroidal potential of radius r_0, supplemented by a Gaussian potential centered at $r = r_0$ (where $r = \sqrt{x^2 + y^2}$), forming an azimuthally symmetric barrier that makes it possible to split

the confinement into an inner and an outer ring:

$$V(\mathbf{r}) = \tfrac{1}{2}M\omega^2\big[(r-r_0)^2 + \lambda^2 z^2 + V_B e^{-(\frac{r-r_0}{\sigma})^2}\big]. \quad (1)$$

The potential has two minima located at $r_1 = r_0 - \sqrt{(}\sigma^2 \ln V_B/\sigma^2)$ and $r_2 = r_0 + \sqrt{(}\sigma^2 \ln V_B/\sigma^2)$. The confinement frequency in the radial plane is given by $\omega/(2\pi)$, while that along z is $\omega_z = \lambda\omega$. The width and strength of the barriers are characterized by the parameters σ and V_B, respectively. In the following, we analyze the rotational properties of dysprosium atoms confined by the above potential. The behavior can be modeled using the usual extended Gross-Pitaevskii equation (eGPE) $i\hbar\partial\psi/\partial t = \delta E[\psi]/\delta\psi^*$ with the corresponding energy functional in the nonrotating frame given by

$$E = \int dV \bigg(\frac{\hbar^2}{2M}|\nabla\psi|^2 + V|\psi|^2 + \frac{1}{2}g|\psi|^4 + \frac{1}{2}g_{\rm dd}|\psi|^2\bigg(\frac{1-3\cos^2\theta}{|\mathbf{r}|^3} * |\psi|^2\bigg) + \frac{2}{5}\gamma|\psi|^5\bigg). \quad (2)$$

In the rotating frame, the above equation reads $E(\Omega) = E - \Omega L$, where Ω is the rotation frequency and $L = \int dV\ \psi^*\hat{L}_z\psi$ is the angular momentum, with $\hat{L}_z = -i\hbar(x\partial_y - y\partial_x)$ being the angular momentum operator. The contact interaction has strength $g = 4\pi\hbar^2 a/M$ and can be tuned by varying the s-wave scattering length a. We denote the particle mass by M. The angle θ is defined as the angle between the position vector and the dipole moment, which is assumed to align with the z-direction. The coefficient of the dipole-dipole interaction (DDI) is $g_{\rm dd} = 4\pi\hbar^2 a_{\rm dd}/M$, where $a_{\rm dd} = \mu_0\mu_m^2 M/12\pi\hbar^2$ represents the dipolar length. The last term in Eq. (2) is the so-called Lee-Huang-Yang (LHY) correction, where $\gamma = \frac{32}{3}g\sqrt{a^3/\pi}(1+\frac{3}{2}\epsilon_{\rm dd}^2)$ and $\epsilon_{\rm dd} = a_{\rm dd}/a$ [80,81]. The ground states are determined by solving the eGPE equation using the split-step Fourier method in imaginary time, while real-time evolution is employed to explore the system's dynamical behavior. We here consider $N = 10\,000$ ^{164}Dy atoms with $a_{\rm dd} = 130a_0$. The trapping frequencies are $(\omega, \omega_z) = (1000, 1700)$ Hz. and the width $\sigma = 10a_{\rm dd}$.

By varying V_B, $\epsilon_{\rm dd}$, and Ω, in the following, we systematically explore both the nonrotational and rotational properties of the system. When Ω exceeds a critical value, JVs and CVs can emerge in the ground state, identified by examining the lowest energy $E(L)$ as a function of angular momentum L (i.e., the so-called yrast line [82]). To do this, we shall minimize $E(L) = E + C(L-L_0)^2$, where C is a large number [76]. The energy for a single component in a toroidal setup can be expressed as the sum of a term quadratic in L, arising from the kinetic energy, and another function primarily originating from particle interactions, which is symmetric and periodic in L when central vortices are generated in the system [2]. A minimum in energy at a value $L = L_0$ indicates a metastable persistent current with angular momentum L_0 in the ground state [2,83–85]. To understand the rotational behavior of the system, we examine both the yrast lines (see, for example, Figs. 3(a), 4(a), and 5) and the angular momentum as a function of Ω (see, for example, Figs. 3(b), 4(b), and 6).

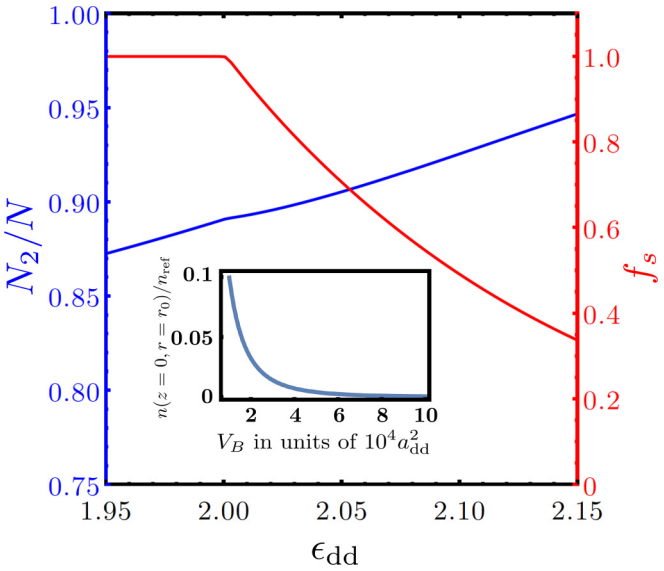


FIG. 2. The relative population, N_2/N [left axis], of the condensate residing in the outer ring and superfluid fraction, f_s, [right axis] as a function of the relative dipolar strength $\epsilon_{\rm dd}$ for a barrier strength $V_B = 10^5 a_{\rm dd}^2$. The inset shows the azimuthal symmetric density, $n(r = r_0, z = 0)$, for $\epsilon_{\rm dd} = 1.95$ as a function of V_B. The reference density, $n_{\rm ref}$, corresponds to the density at $r = r_0$ and $z = 0$ when $V_B = 0$.

III. RESULTS AND DISCUSSIONS

A. Nonrotating ground states

Let us first highlight the static ground state properties of the double-ring system, initially focusing on barrier strength $V_B = 10^5 a_{\rm dd}^2$, which separates the rings without any density overlap between them. The density configurations are determined by how the dipolar atoms are distributed within the two rings. The particle number of the outer rings, $N_2 = \int_{r>r_0} dV|\psi|^2$, is shown as a function of $\epsilon_{\rm dd}$ in Fig. 2. It indicates that the outer ring always has a higher population (see also Fig. 1), increasing further as the dipolar interaction becomes stronger. This behavior can be understood by considering both the long-range nature of interactions between the atoms and the underlying confining potential. The dipolar atoms experience repulsion in the x-y plane and attraction along the polarization axis. To minimize repulsion and, consequently, the total energy, it is energetically favorable for the atoms to occupy the ring with a larger radius. However, placing all the atoms there would enhance both the potential energy and the total energy of the system. Consequently, the density in the inner ring remains nonzero. The smaller the value of $\epsilon_{\rm dd}$, the more particles it contains.

The imbalance of population also determines if (and how) the density modulation emerges. For smaller $\epsilon_{\rm dd}$, the system is expectedly in the SF regime. A representative 3D density isosurface of such a state at $\epsilon_{\rm dd} = 1.95$ is shown in Fig. 1(a). (Note that here, the phase is constant.) Earlier studies in a simply connected confinement potential have demonstrated that at a fixed interaction strength, for increasing particle number, the formation of the SS state is favored [58–60]. Owing to its larger population, the condensate in the outer ring becomes

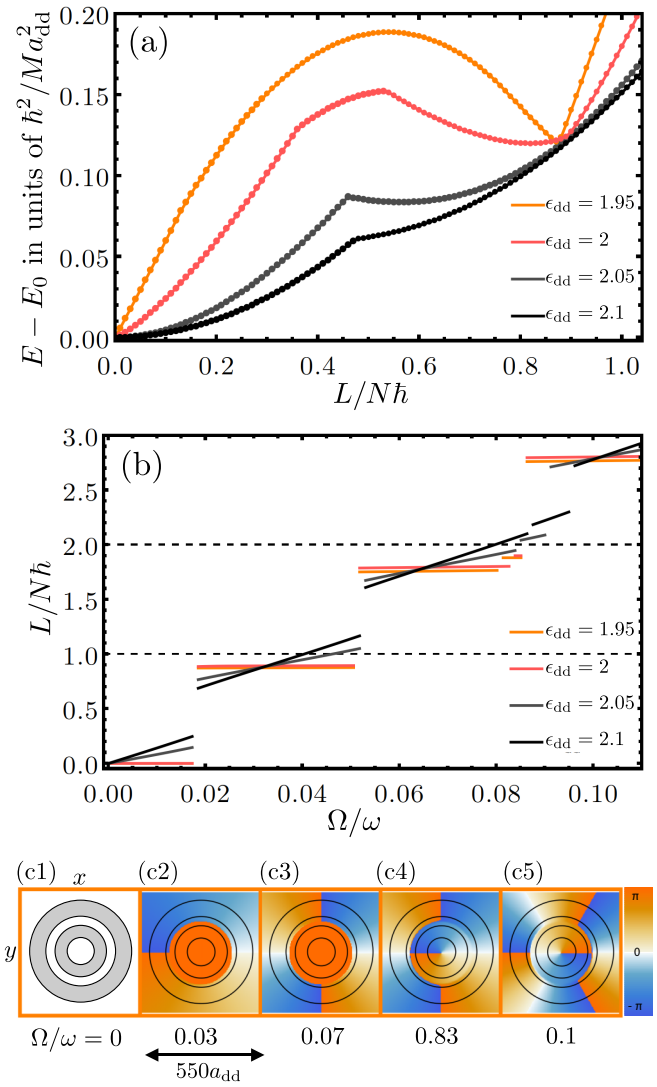


FIG. 3. Rotational properties of the double-ring dipolar system with the barrier strength $V_B = 10^5 a_{dd}^2$ for different values of interaction parameters ϵ_{dd} [see the legends]. (a) Ground state $E(L)$ relative to the nonrotating ground state E_0 as a function of total angular momentum L of the system. (b) Angular momenta L as a function of rotation frequency Ω. The dashed lines indicate the integer values of L expected for a central vortex. (c1)–(c5) The two-dimensional phase profile in the plane of the rings [at $z = 0$] for different values of Ω for a specific $\epsilon_{dd} = 1.95$. The black line indicates the density contours taken at a value of 1/30 of the maximum density corresponding to each profile. The rotation frequencies are given below each plot. For (c1), the phase is constant, and the regions where the inner and outer condensates are present are shaded in grey for clarity. The corresponding states are: (c1) no vortex; (c2) JV_1; (c3) $2JV_1$s; (c4) $CV + JV_1$; and (c5) $2JV_1$s + CV.

more prone to a periodic density modulation (similar to the one in Fig. 1(c), but with uniform phase) as ϵ_{dd} increases. For a quantitative analysis of the phase transition, we calculate the superfluid fraction, $f_s = 1 - I/I_c$, where $I = \lim_{\Omega\to 0} L/\Omega$ [61,86]. The classical moment of inertia $I_c = M\langle r^2\rangle$ is obtained from the ground state. The f_s as a function of ϵ_{dd} is shown in Fig. 2(a) for the parameters specified above. For $\epsilon_{dd} \lesssim 2.0$, we have $f_s = 1$, as expected, for the SF. For larger values of ϵ_{dd}, the ground state is an SS, with the outer ring showing nine density maxima for dipolar strength in the interval $2.15 \geqslant \epsilon_{dd} \gtrsim 2.078$. The number of localized density sites can be systematically controlled by scaling both N and r_0 such that N/r_0 remains constant, while all other parameters are kept fixed. We note that considering larger r_0, and decreasing $r_2 - r_1$, the density modulation may occur in both rings. However, we restrict our analysis to the scenario of density modulation forming only in the outer ring. We also note that for atoms with only short-range interactions, it is possible to have almost an equal number of atoms in both rings [38], but intrinsic density modulations forming an SS do not develop in these systems.

Examining the role of the Gaussian barrier, we find that, within the range $V_B = (10^4 - 10^5)a_{dd}^2$, its impact on the superfluid fraction and the corresponding phase transition is weak. Specifically, for $V_B = 10^4 a_{dd}^2$, the eight-fold modulated state becomes energetically favorable for $2.15 \geqslant \epsilon_{dd} \gtrsim 2.078$. A smaller value of V_B leads to a density overlap between the rings along the radial direction; see the inset of Fig. 2, where we have shown the density at the position of the barrier for varying barrier strength V_B. As we will discuss in the subsequent section, when the system is set into rotation, such finite density at the azimuthal barrier significantly influences the vortex position and thus the angular momentum of the system.

B. Rotational ground states

Let us now investigate the rotational properties of the system to understand how the inter-ring connection determines which part of the system acquires angular momentum and how it influences the nucleation of topological defects.

1. Separated rings

We first discuss the case in which the rings are completely separated by a barrier of strength $V_B = 10^5 a_{dd}^2$. By analyzing the energy as a function of angular momentum [Fig. 3(a)], the angular momentum as a function of rotation frequency [Fig. 3(b)], and the spatial phase distributions [Figs. 3(c1)–3(c5)], we can effectively characterize the existence of persistent currents in the ground state and the vortex nucleation. For the SF state at $\epsilon_{dd} = 1.95$, the yrast line $E(L)$ exhibits the characteristic downward cusp, i.e., a V-shaped minimum, at $L/N\hbar \approx 0.87$, identifying the state that can host a persistent current [orange line in Fig. 3(a)]. This is further validated by calculating the ground state in the rotating frame, and analyzing the L vs Ω behavior, which exhibits a sudden jump in angular momentum to $L \approx 0.87N\hbar$ at the critical rotation frequency $\Omega = 0.018\omega$, as shown in [Fig. 3(b)]. Notably, this value matches the fraction of particles in the outer ring $N_2/N = 0.87$, indicating that angular momentum is carried by it. This becomes evident from Fig. 3(c2), where a representative two-dimensional phase profile at $\Omega = 0.03\omega$, reveals a uniform phase in the inner ring, while the outer ring exhibits a full 2π winding. This suggests that a vortex resides at the junction between the rings. It is identified as a JV_1 in the rotating ground state. In the SF state, the wave function of

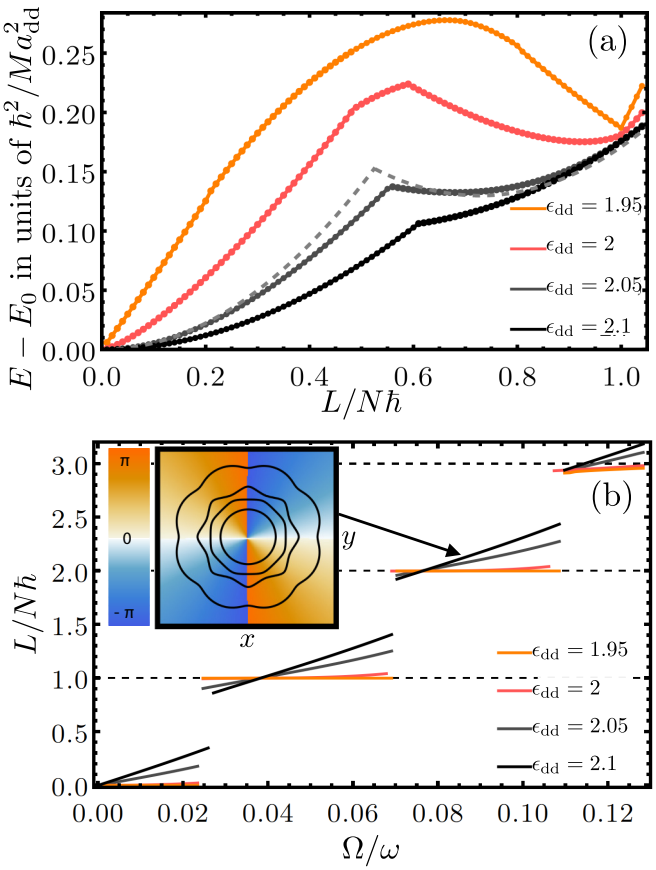


FIG. 4. Rotational states of double-ring dipolar system with a barrier strength $V_B = 10^4 a_{dd}^2$ for different ϵ_{dd} [see the legends] (a) Energy dispersion relation $E(L)$ relative to the nonrotating ground state E_0 as a function of angular momentum per particle. The points are calculated from the fixed angular momentum routine, and the dashed line shows Eq. (8), where we have used the state $\psi(L = 0)$ for the expectation value. (b) Angular momentum L of the rotational ground state realized at various rotation frequencies Ω. The inset shows the phase profile with the density contour [value being 1/30 times the maximum density] for $\epsilon_{dd} = 2.1$ at a specific rotation frequency $\Omega = 0.09\omega$ corresponding to 2CVs.

a JV_1 located at position $\mathbf{r}_{JV_1}$ can be expressed as

$$\psi_{JV_1}(\mathbf{r}) = \sqrt{n(\mathbf{r})} \begin{cases} e^{i(\phi+\pi)}, & r > r_0 \\ e^{i\angle(\mathbf{r}_1, \mathbf{r}_{JV_1})}, & r < r_0 \end{cases}. \tag{3}$$

Here, the term $\angle(\mathbf{r}_1, \mathbf{r}_{JV_1})$ represents the angle between $\mathbf{r}_{JV_1}$ and the reference vector $\mathbf{r}_1 = (1, 0)^T$. This expression is only valid when the density at $r = r_0$ vanishes to ensure the continuity of the wave function. The phase of the inner ring is inherently linked to the position of the JV_1. Specifically, at the location of the JV_1, the phase of the wave function has a jump of π in the radial direction.

Energy minima in the yrast line [only one is shown here for brevity] correspond to a metastable state where persistent current can be created within a specific range of rotation frequencies. For instance, the next state, appearing for $\Omega > 0.051\omega$, has $L = 2N_2\hbar$, and accommodates two JV_1s [Fig. 3(c3)]. A particularly intriguing transition occurs at $\Omega = 0.081\omega$, when one JV_1 migrates to the center, giving rise to a state that hosts both a JV_1 and a CV [Fig. 3(c4)]. In this configuration, each particle in the inner ring acquires superfluid circulation, leading to $L = (N_2 + N)\hbar$. Similarly, by further increasing the Ω, it is possible to create a system that supports multiples JV_1s and CVs [see Fig. 3(c5) for two JV_1s and one CV].

In the SS state ($\epsilon_{dd} > 2.078$), the minimum of the yrast line shifts to a lower value of $L/N\hbar$. For smaller angular momentum, the variation of energy is more parabolic in nature for larger ϵ_{dd} in contrast to the linear variation that we observe in SF. Moreover, a kink appears at $L = N_2\hbar/2$ due to the intersection of two energy branches arising from the system's kinetic energy. Notably, while in a single-ring SS, the kink location at $L = N\hbar/2$ remains unchanged and is determined solely by the total number of particles, in a double-ring system it shifts toward $N/2$ as the outer ring progressively becomes more populated for larger ϵ_{dd}; see $\epsilon_{dd} = 2.05$ and 2.1 in Fig. 3(a). The energy barrier that prevents the metastable state from decaying into the nonrotating state also depends on f_s; compare the range between $\epsilon_{dd} = 2.1$ and 2.05. Additionally, in the angular momentum of the ground states, we observe a gradual slope linked to the value of f_s before it abruptly jumps to a higher value with increasing rotation frequency. While the rotational states for different ϵ_{dd} exhibit the same number of JV_1s and CVs, their critical rotation frequencies differ due to a varying population in the outer ring. If the superfluid fraction drops below a critical threshold, vortices can still nucleate in the rotating ground state; however, they do not generate a persistent current, causing the system to decay into a nonrotating state in the dynamics once Ω is reduced to zero.

Near the phase transition in the nonrotating ground state on the SF side, we observe that rotation can induce density modulation, driving the system into the SS phase. This effect is evident for $\epsilon_{dd} = 2$. The yrast line reveals that the condensate remains in the SS phase within the interval $0 < L/N\hbar < 0.35$ and for $L/N\hbar > 0.54$. However, when the energy connected to the rigid body rotation of the SS becomes large, it is energetically favorable to transform the system back to an SF state. Thus, the yrast line retains a concave segment for $0.36 < L/N\hbar < 0.54$. But the metastable state at $L/N\hbar = 0.82$ lies in an SS phase hosting a JV_1. The density modulations, though present in the outer ring, are not pronounced enough (compared to others) to generate a discernible slope in the L vs Ω plot in Fig. 3(b).

2. *Connected rings*

The observation of JV_1 becomes possible because the density drops to zero at the location of a strong barrier. A weak barrier that maintains a nonzero density between the rings favors the formation of a vortex at $r < r_0$. The overall behavior of the yrast lines, which support persistent currents at their minima and display kinks in the SS regime, is similar to the case of separated rings [compare Figs. 3(a) and 4(a)]. In particular, we highlight the behavior for $\epsilon_{dd} = 2.1$ when $f_s = 0.490$. The absence of a minimum in the yrast line indicates that persistent currents cannot form in this system. Nevertheless, the rotational ground states can still host vortices [Fig. 4(b)].

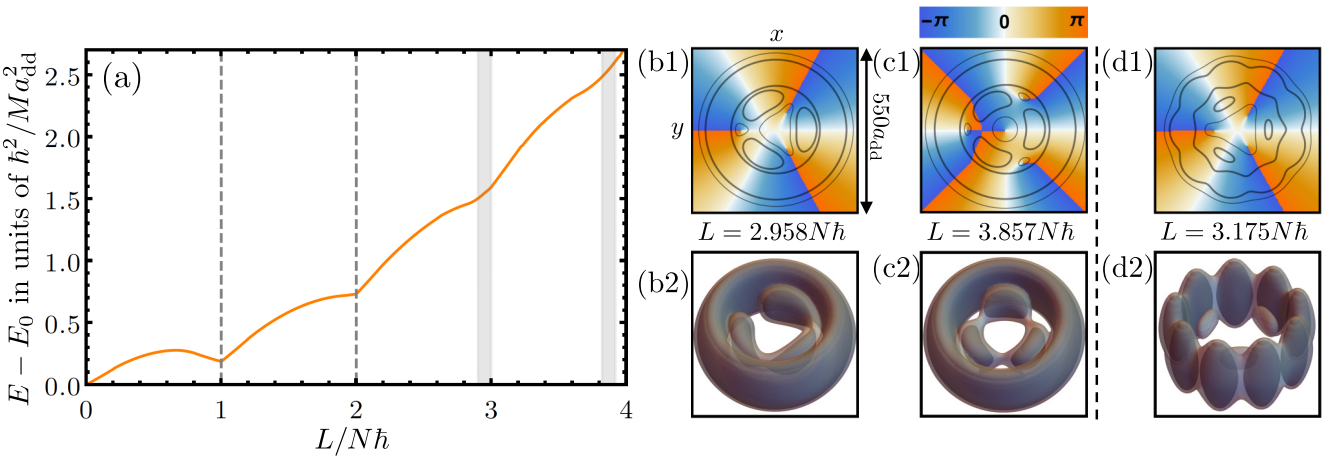


FIG. 5. The formation of density modulation in the inner ring and the SF-SS phase transition induced by rotation for $V_B = 10^4 a_{dd}^2$ (a) Energy $E(L)$ as a function of angular momenta L relative to the non-rotating ground state energy E_0 for $\epsilon_{dd} = 1.95$. The dashed lines indicate the angular momenta of the global minimum in the rotating frame, where the ground states are in the SF phase. The gray-shaded area represents all angular momenta corresponding to the SS ground states. Shown also the phase profiles in the plane $z = 0$ [(b1), (c1), (d1)] and three dimensional density isosurfaces [(b2), (c2), (d2)] for $\epsilon_{dd} = 1.95$ [(b1), (b2), (c1), (c2)] with (b1), (b2) $L/N\hbar = 2.958$ (3 JV_2s) and (c1), (c2) $L/N\hbar = 3.857$ (CV + 3JV_2s), and (d1), (d2) for $\epsilon_{dd} = 2.1$ with $L/N\hbar = 3.175$ (3 JV_2s). The density contour lines correspond to a value of 20% and 1% of the maximum density [(b1), (c1), (d1)]. The isosurfaces are taken at 10% and 20% of the maximum densities in (b2) and (c2) and at 3% and 10% of the maximum density in (d2).

Depending on the rotation frequency Ω, the vortex may manifest either as a CV or as a different type of JV distinct from JV_1. That the vortex is a CV within the interval $0.024\omega < \Omega < 0.108\omega$ is evident from the integer value of the angular momentum, shared by all particles in the condensate, for $\epsilon_{dd} = 1.95$ [see Fig. 4(b)]. In the SS regime, the same vortex remains a CV, though with a reduced superfluid angular momentum. The critical rotation frequencies for the system at which the charge of the CV changes from $q - 1$ to q are given as the solutions of the transcendental equation

$$\Omega = \frac{\hbar\langle r^{-2}\rangle}{M}\left(q - \frac{1}{2}\right). \tag{4}$$

We note that the mean value is calculated from the wave function which, in general, depends on all parameters of the system.

Let us now analyze the shape of the yrast line. The E is linear for small values of L and around the minima. We can understand the behavior at small L by assuming that the vortex is far from the condensate, such that its core does not interfere with the condensate density. In this scenario, the wave function can be approximated as

$$\psi = \sqrt{n(\mathbf{r})}\exp\left[i\tan^{-1}\left(\frac{y}{x - x_0}\right)\right], \tag{5}$$

where we assume the vortex to enter on the x-axis, such that its position in the xy-plane is given by $(x_0, 0)$, and $n(\mathbf{r})$ is the local density. Inserting Eq. (5) in the energy functional and expanding linearly around $L = 0$, we obtain

$$E - E_0 \approx E_{kin} = \frac{\hbar NL}{2M\langle r^2\rangle}, \tag{6}$$

which is valid as long as $x_0^2 \gg \langle r^2\rangle$. To understand the linear behavior near the minimum energy, where the vortex is located at the center and the interaction between the vortex and condensate can be neglected, we again take Eq. (5) as an ansatz and expand linearly around $L = N\hbar$:

$$E - E_0 \approx E_{kin} = \frac{\hbar^2}{2M}\langle r^{-2}\rangle + \frac{\hbar}{M}(L - N\hbar)\frac{\langle x/r^4\rangle}{\langle x/r^2\rangle}. \tag{7}$$

For arbitrary values of L, the energy of the vortex consists of two parts: the kinetic energy and the interaction energy, which arises from the density depletion when the vortex penetrates the condensate. The latter is a concave parabolic function of L. While Eqs. (6) and (7) can qualitatively capture the linear behavior in the SF state, a quantitative agreement requires considering the deep SF regime or a nondipolar superfluid characterized by dominant short-range interactions. For an SS, the situation is entirely different. An additional term in the kinetic energy emerges from the solid body rotation, reading as $E_{SS} = L^2/2I_{sb}$ where $I_{sb} = (1 - f_s)M\langle r^2\rangle$. The contribution of the interaction energy decreases with decreasing f_s, because the vortex can pass through the interstitial region between the density maxima and therefore minimize the interaction.

In order to calculate the yrast line for the SS state, let us decompose the total angular momentum L into two parts, namely a SF part $L_{SF} = f_s N\hbar$ and an SS part $L_{SS} = L - L_{SF}$. The yrast line can then be constructed by

$$E(L) = \min\left[E_{SS}(L), E_{SS}(L_{SS}) + f_s\frac{\hbar^2}{2M}\langle r^{-2}\rangle\right]. \tag{8}$$

In Fig. 4(a), the E(L) is plotted (see the dashed line) using Eq. (8) for $\epsilon_{dd} = 2.05$, where we have calculated the corresponding expectation values using $L = 0$. The function [Eq. (8)] agrees well with the exact yrast line. This shows that the yrast line of a supersolid is determined by the superfluid fraction together with the particle density, and the interactions

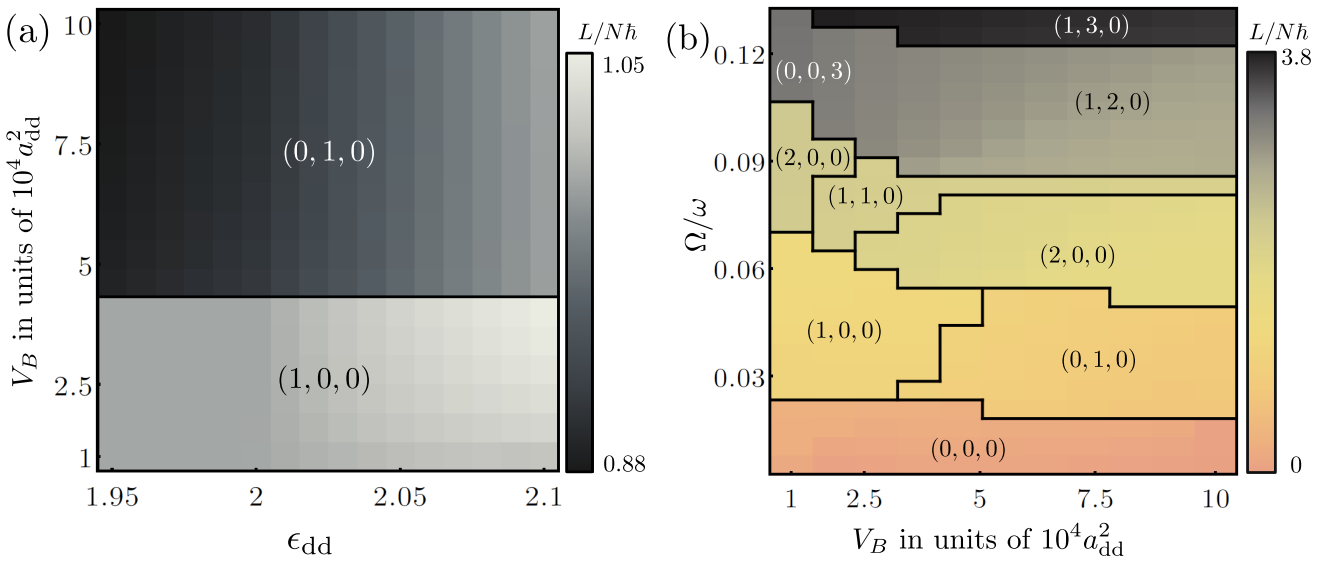


FIG. 6. Angular momentum (a) as a function of barrier strength V_B and interaction strength ϵ_{dd} at a fixed rotation frequency $\Omega = 0.04\omega$, and (b) as a function of barrier strength V_B and rotation frequency Ω at fixed $\epsilon_{dd} = 2$. Each state in the phase diagram is labeled by the charges q_i of the topological defects $(q_{CV}, q_{JV_1}, q_{JV_2})$.

play a minor role. The yrast line has a kink at

$$L/N\hbar = f_s/2 + (1 - f_s)\langle r^2\rangle\langle r^{-2}\rangle/2N^2 .$$

Further, the yrast line has a metastable state at $L = f_s N\hbar$ as long as $f_s > f_s^c$, where $f_s^c = \langle r^2\rangle\langle r^{-2}\rangle/(N^2 + \langle r^2\rangle\langle r^{-2}\rangle)$. For the $\epsilon_{dd} = 2.1$, $f_s^c = 0.533$ and $f_s = 0.493$, and therefore a no-metastable state is observed in Fig. 4(b). We also point out that all equations mentioned above are also valid for the yrast lines of the separated ring cases if we exchange N, $\langle ...\rangle$ and f_s by N_2, $\langle ...\rangle_2$ and $f_{s,2}$, where $\langle ...\rangle_2$ means integration over the outer ring only and $f_{s,2}$ is the superfluid fraction of the outer ring. The latter can be obtained by calculating the angular momentum and the moment of inertia for the outer ring only. Furthermore, for a single-ring system with tight confinement and localized density, the relation $\langle r^2\rangle\langle r^{-2}\rangle \sim 1$ holds, indicating that the kink appears at $L/N\hbar = 1/2$. In contrast, for the double-ring system, the kink position can be varied significantly by tuning ϵ_{dd} and V_B, thereby allowing the system to host a wider range of vortex configurations.

The most intriguing effects of the connected-ring geometry emerge at high angular momentum states. At these higher angular momentum states, rotation alone induces density modulation in the inner condensate, transforming it into an SS state with three localized density sites. The presence of SS is reflected in the slope of the angular momentum, detectable even for $\epsilon_{dd} < 2$; see Fig. 4(b). To gain deeper insight into this phenomenon, we calculate the yrast line up to high angular momentum states, $L/N\hbar = 4$, for $\epsilon_{dd} = 1.95$ [Fig. 5(a)]. Two types of topological defects can be identified in the dispersion relation. The first two dashed lines, indicating kinks at $L/N\hbar = 1, 2$, correspond to CVs. In any rotating frame, $E - L\Omega$, the positions of these kinks remain fixed. Additionally, we observe two defects with angular momenta indicated by the gray regions. In a rotating frame, these defects can form a global minimum at values L_0, which satisfy $\partial E/\partial L|_{L=L_0} = \Omega$, meaning that the position of the minimum depends on the rotation frequency at which the vortices are nucleated. This behavior is possible only if solid-body rotation occurs due to the formation of localized density sites, with the associated vortices being JV_2s, which form at the junctions between these sites. The ensuing sites and three JV_2s at the junctions between these sites for $\epsilon_{dd} = 1.95$ and $\epsilon_{dd} = 2.1$ are shown in Figs. 5(b1), 5(b2), 5(d1), and 5(d2), respectively. These are the stationary states for a fixed value of the angular momenta. The one with $\epsilon_{dd} = 2.1$ corresponds to the SS with a density modulation in both inner and outer rings. We show that adding the next vortex as a CV is energetically favorable if the angular momentum becomes larger, such as $L/N\hbar = 3.857$ [Figs. 5(c1) and 5(c2)], and thus, enabling the coexistence of CV and JV_2. We note that the rotation-induced SS also occurs in a single-ring configuration [76] and arises from the fact that, in the rotating frame, the energy at the roton minimum can satisfy the condition $E_{rot} - \Omega L \leqslant 0$ by tuning Ω. Notably, this provides an alternative protocol for generating an SS state, independent of controlling ϵ_{dd}. This mechanism is particularly relevant in our double-ring system, where modulation can appear in either the outer or inner ring, depending on the presence of an inter-ring density connection. The emergence of modulation in the inner ring is intrinsically linked to the JV_2s and represents one of the key highlights of our work.

3. Phase diagrams

We present the nucleation of distinct topological structures as a function of system parameters, V_B, ϵ_{dd}, and Ω delineated in the two phase diagrams shown in Fig. 6. The parameters, N, (ω, ω_z), and r_0 are kept fixed. The total charge associated with each vortex type is denoted by q_c, where $c \in \{CV, JV_1, JV_2\}$. A given configuration is represented by the charge tuple $(q_{CV}, q_{JV_1}, q_{JV_2})$. First, we examine how the Gaussian barrier influences the presence of JV_1s and CVs for different interaction strengths ϵ_{dd}. We fix the rotation frequency at $\Omega = 0.04\omega$ and calculate the total angular momentum as a function of V_B

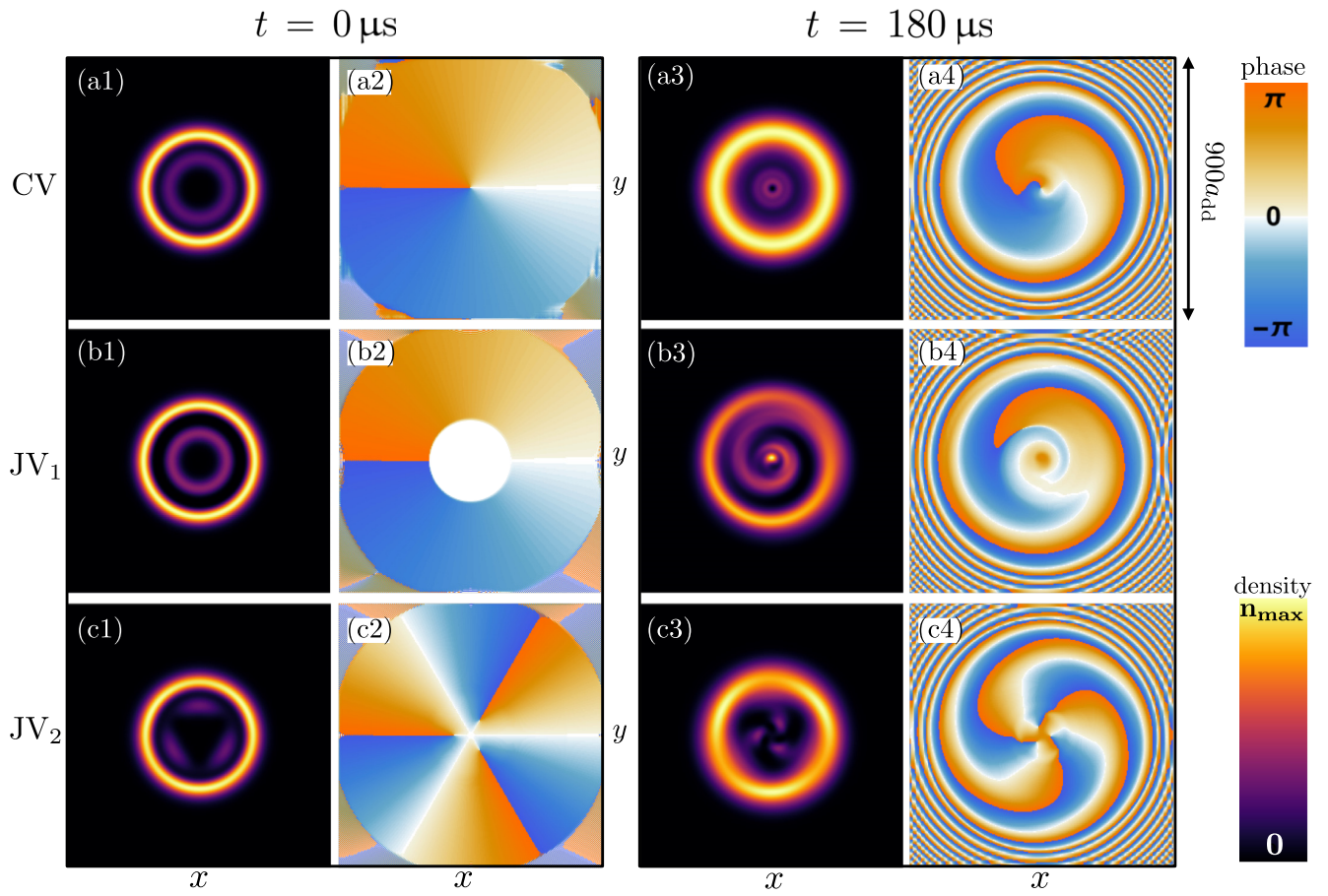


FIG. 7. Interferometric protocol for detection of (a1)–(a4) CV, (b1)–(b4) JV_1, and (c1)–(c4) JV_2. Shown here two dimensional density $n_{2D}(x, y)$ [(a1), (b1), (c1), (a3), (b3), (c3)] and phase profiles [(a2), (b2), (c2), (a4), (b4), (c4)] at $z = 0$ in the dipolar double-ring system at $t = 0$ [(a1), (a2), (b1), (b2), (c1), (c2)] and $t = 180\,\mu s$ [(a3), (a4), (b3), (b4), (c3), (c4)]. After preparing the initial states, all the confinement potentials are set to zero for $t > 0$. The initial condensates have an interaction strength of $\epsilon_{dd} = 1.95$, rotation frequencies of $\Omega/\omega = 0.04,\ 0.04,\ 0.1$, and $V_B = 10^4 a_{dd}^2,\ 10^5 a_{dd}^2,\ 10^5 a_{dd}^2$ for CV, JV_1, and JV_2.

and ϵ_{dd}, as shown in Fig. 6(a). For the chosen value of Ω, CVs exist when $L \geqslant N\hbar$, while JV_1s are present when $L < N\hbar$. We observe a critical barrier strength $V_{B,c} \approx 3.3 \times 10^4 a_{dd}^2$ that separates the two regions, $(0, 1, 0)$ and $(1, 0, 0)$, of the phase diagram, indicating a single JV_1 and a single CV. By comparing this with the inset in Fig. 2, we see that the density for $V_{B,c}$ is nonzero. Consequently, the creation of the JV_1-core requires kinetic energy, but still the total energy of the JV_1 is smaller than the total kinetic energy of a CV. For the parameter grids in Fig. 6(a), we do not see a dependency of ϵ_{dd} on $V_{B,c}$. The SF-SS phase transition is also evident in Fig. 6. For $\epsilon_{dd} \leqslant 2$, in the SF state, the angular momentum of the CV is constant and equal to $N\hbar$. In the SS phase, the angular momentum of the CV is no longer constant due to the contribution from the solid part of the system, which increases with larger ϵ_{dd}. In the case of a JV_1, this effect is reinforced by the increasing population of the outer ring. This result once again confirms that the barrier is the cause for the nucleation of JV_1s.

Next, we fix the interaction strength to $\epsilon_{dd} = 2$ and calculate the angular momentum of the system for different values of Ω and V_B to identify various vortex configurations; see Fig. 6(b). Typically, CVs are energetically favored at low barrier strengths V_B, while JV_1 states become preferred as V_B increases, see, for example, in the regime $(0.03 < \Omega/\omega < 0.05)$. This behavior is consistent with Figs. 3, 4, and 6(a). As the rotation frequency increases, a JV_1 can coexist with a CV even at relatively small V_B. Notably, the minimal barrier strength required for such a configuration, $(1, 1, 0)$, is $V_{B,c} \approx 1.9 \times 10^4 a_{dd}^2$ [Fig. 6(b)]. We notice that transitions between configurations with different numbers of JV_1 and CV excitations occur sharply as a function of both V_B and Ω, due to the clear distinguishability of their preferred locations in the double-ring system. Remarkably, the above-mentioned transition is no longer sharp when the system involves a JV_2; see, for example, the angular momenta as the system crosses over from the $(0, 0, 3)$ to the $(1, 2, 0)$ state. In this regime, as the barrier strength is gradually increased for a fixed Ω, say $0.12\,\omega$, two of the three JV_2 excitations move to $r = r_0$, while one JV_2 moves to $r = 0$. For $\epsilon_{dd} = 2$, the nonrotating ground state lies close to the phase transition on the SF side. While nucleating the $(0, 0, 3)$ configuration, the inner ring develops a density modulation, which steadily fades as V_B increases. Consequently, the total angular momentum gradually

decreases from approximately $2.96N\hbar$ to $2.81N\hbar$. Eventually, in the strong barrier regime, this vortex configuration evolves into the (1, 2, 0) state.

C. Vortex detection

In the preceding sections, we have demonstrated how JVs and CVs can be nucleated in a double-ring system. This system is particularly advantageous as it provides a practical method for detecting these vortices once they are generated. The corresponding protocol involves interfering condensate parts located in the inner and outer rings by switching off the trap and monitoring the resulting interference pattern. Since JVs and CVs exhibit distinct phase profiles, they are expected to produce discernible density patterns during expansion. We illustrate such expansion dynamics in Fig. 7, focusing only on SF with $\epsilon_{\rm dd} = 1.95$.

The initial 2D density profiles $n_{\rm 2D}(x, y)$ and phase profile for a CV are highlighted in Figs. 7(a1) and 7(a2), respectively. Such an initial state is created with $V_B = 10^4 a_{\rm dd}^2$ and $\Omega = 0.04\omega$. Here, both the inner and outer condensates contain one complete phase winding, resulting in concentric circular density patterns after interference [Figs. 7(a3) and 7(a4)]. Such density and phase profiles have to be contrasted when a $\rm JV_1$ is present in the system for $V_B = 10^5 a_{\rm dd}^2$; see Figs. 7(b1)–7(b4). The inner ring possesses a uniform phase whereas the phase winds over 2π in the outer ring owing to single $\rm JV_1$. Consequently, after interference, the density develops a single spiral around the center. However, the presence of density modulation in the inner ring, which is otherwise an SF in the absence of rotation, indicates the existence of $\rm JV_2$s. This is further confirmed by the interference pattern, where we observe that modulated density structures persist in the inner region of the condensate, with the $\rm JV_2$s located between these structures [Figs. 7(c3) and 7(c4)]. We remark that, while our results on interference dynamics are illustrated using a specific set of parameters and focus on short timescales to avoid boundary effects, the phenomena remain observable over longer durations and are generally applicable, with the timescales being adjustable via the trapping frequencies. Thus, this interference protocol not only confirms the existence of a defect but also reveals the phase distribution resulting from its specific position.

IV. CONCLUSIONS

In conclusion, we have investigated the nonrotational and rotational properties of dipolar atoms in coplanar and concentric double rings. We have specifically focused on two different cases: one where the rings are connected by density overlap, and another where they are separated. Our findings reveal a population imbalance between the inner and outer rings, in contrast to nondipolar systems. Notably, the outer ring exhibits a proclivity for spontaneous density modulation, indicative of an SS state, regardless of the strength of the barrier forming the double-ring structure.

We have studied the rotational properties of the system and demonstrated the existence of a persistent current by calculating its energy as a function of angular momentum. The persistent current is accompanied by the formation of topological structures, specifically $\rm JV_1$ and CV, which appear in the separated and connected rings, respectively. We have delineated their regions of existence in a diagram by calculating angular momentum as a function of interaction and barrier strength. Specifically, we have identified multiple topological defects, such as $\rm JV_1$s and combination of CV and $\rm JV_1$, which emerge in the separated ring case at higher rotational frequencies.

One of the intriguing features of our system lies in its connection to rotation-induced SS state formation. We have found that, for relatively small angular momentum, rotation can induce density modulation in the outer ring, transforming an otherwise SF state into an SS state. Interestingly, in the case of connected rings, the inner condensate forms three localized density sites at high angular momentum states, where three vortices are nucleated at the junctions between the localized density sites. These vortices, which we refer to as $\rm JV_2$, are associated with the spontaneously formed localized density sites induced by rotation and are unique to our double-ring dipolar system. Finally, by utilizing an interferometric protocol, we have demonstrated how these different topological structures can be detected in the experiment.

There are several extensions of the present work worth pursuing in future research. A straightforward extension would be to study the underlying collective excitation spectra of the double-ring system, particularly around the critical point of the phase transition. Additionally, it would be interesting to explore the signature of $\rm JV_2$ in the excitation spectrum. Another intriguing direction would be to investigate the parameter regime where density modulation occurs in both rings in the nonrotating supersolid state. This would enable the study of shear-wave propagation across the azimuth of the rings by suddenly altering the distance between the inter-ring localized density sites. Furthermore, investigating finite-temperature properties [87] and the effects arising when dipole moments are tilted with respect to the perpendicular axis in the context of this setup would be equally compelling.

ACKNOWLEDGMENTS

We thank Thomas Bland, Philipp Stürmer, Tiziano Arnone Cardinale, Deepak Gaur, Lila Chergui, and the Stuttgart Dipolar Gases group for fruitful discussions. We also thank M. Nillson Tengstrand for his help with the eGPE code. M.S., K.M., and S.M.R. acknowledge financial support from the Knut and Alice Wallenberg Foundation (Grants No. KAW 2018.0217 and No. KAW2023.0322) and the Swedish Research Council (Grant No. 2022-03654). T.P. acknowledges support from the European Research Council (ERC) (Grant Agreement No. 101019739).

DATA AVAILABILITY

The data that support the findings of this article are not publicly available. The data are available from the authors upon reasonable request.

APPENDIX A: COMPUTATIONAL DETAILS

Here, we detail the numerical simulations used to obtain the results described in the main text. We numerically

solve the extended Gross-Pitaevskii equation (eGPE) obtained from the functional derivative of the energy density function. The eGPE equation is cast into a dimensionless form in our simulations by rescaling the length and the time by the length scale and the time scale, $l_s = a_{\rm dd}$ and $t_s = Ma_{\rm dd}^2/\hbar$, respectively. Thereafter, we employ the split-time Fourier spectral method to solve the resulting equation [88,89]. The stationary state of the system is obtained through imaginary time propagation, while the dynamical simulation is performed in real time. At each imaginary time step, we preserve the normalization of the wave function, and convergence is reached when the relative deviation of the wave function $\psi(x,t)$ at every grid point and the angular momentum L and energy E between consecutive time steps are smaller than 10^{-6} and 10^{-15}, respectively. It should be noted that calculating the stationary state solution of the eGPE is an involved task due to many closely lying local minima in the energy surface, which necessitates extensive sampling over many different initial conditions to identify the most probable lowest-energy solutions. The mean-field dipolar potential is efficiently evaluated via Fourier transforms, incorporating a spherical cutoff, set to half the box size to prevent spurious interactions between periodic images. Our simulations are carried out in a 3D box characterized by a grid $(n_x \times n_y \times n_z)$ corresponding to $(128 \times 128 \times 64)$ $(512 \times 512 \times 128$ for the simulation of interferometric protocol). The employed spatial discretizations (grid spacing) refers to $\Delta_i = l/n_i$ with $l = 900$ for the calculations of rotating and non-rotating ground states ($l = 1500$ for the simulations of interferometric protocol), while the time step of the numerical integration is $\Delta_t = 10^{-2}$.

APPENDIX B: DERIVATION OF EQS. (6) AND (7)

To arrive at Eqs. (6) and (7), we calculate the angular momentum as a function of the position of the vortex x_0:

$$L = \langle \hat{L}_z \rangle = \hbar \int dV\, n\, \frac{x^2 - xx_0 + y^2}{x^2 - 2xx_0 + x_0^2 + y^2}. \tag{B1}$$

When $L \to 0$, the vortex is far away from the condensate. In this case, the angular momentum can be approximated as $L = \hbar\langle r^2\rangle/x_0^2$. To obtain this expression, we have assumed $\langle x\rangle = 0$, which holds since the vortex and condensate are well separated. The kinetic energy can be calculated via Eq. (2). For large x_0, we obtain $E(L) - E_0 \approx E_{\rm kin} - E_0 = N\hbar^2/(2Mx_0^2)$, where $E_0 = E[\sqrt{n}]$. Combining these two expressions yields Eq. (6). For $L \to N\hbar$, we expand the angular momentum as $L = N\hbar + \hbar\langle x\rangle x_0/r^2$. The expectation value $\langle x\rangle$ is nonzero because the condensate and vortex are not well separated for angular momenta close to, but not equal to, unity. This holds only if the angular momentum is interpreted as the superfluid angular momentum $L_{\rm SF}$. Combining this with the kinetic energy expression $E_{\rm kin} = \hbar^2\langle r^{-2}\rangle/(2M) + \hbar^2 x_0\langle x/r^4\rangle/M$ yields Eq. (7).

[1] E. P. Gross, Unified theory of interacting bosons, Phys. Rev. **106**, 161 (1957).
[2] F. Bloch, Superfluidity in a ring, Phys. Rev. A **7**, 2187 (1973).
[3] A. J. Leggett, Superfluidity, Rev. Mod. Phys. **71**, S318 (1999).
[4] A. L. Fetter, Rotating trapped Bose-Einstein condensates, Rev. Mod. Phys. **81**, 647 (2009).
[5] F. Bloch, Off-diagonal long-range order and persistent currents in a hollow cylinder, Phys. Rev. **137**, A787 (1965).
[6] K. A. Matveev, A. I. Larkin, and L. I. Glazman, Persistent current in superconducting nanorings, Phys. Rev. Lett. **89**, 096802 (2002).
[7] C. Ryu, M. F. Andersen, P. Cladé, V. Natarajan, K. Helmerson, and W. D. Phillips, Observation of persistent flow of a Bose-Einstein condensate in a toroidal trap, Phys. Rev. Lett. **99**, 260401 (2007).
[8] A. Ramanathan, K. C. Wright, S. R. Muniz, M. Zelan, W. T. Hill, C. J. Lobb, K. Helmerson, W. D. Phillips, and G. K. Campbell, Superflow in a toroidal Bose-Einstein condensate: An atom circuit with a tunable weak link, Phys. Rev. Lett. **106**, 130401 (2011).
[9] S. Moulder, S. Beattie, R. P. Smith, N. Tammuz, and Z. Hadzibabic, Quantized supercurrent decay in an annular Bose-Einstein condensate, Phys. Rev. A **86**, 013629 (2012).
[10] K. C. Wright, R. B. Blakestad, C. J. Lobb, W. D. Phillips, and G. K. Campbell, Driving phase slips in a superfluid atom circuit with a rotating weak link, Phys. Rev. Lett. **110**, 025302 (2013).
[11] S. Beattie, S. Moulder, R. J. Fletcher, and Z. Hadzibabic, Persistent currents in spinor condensates, Phys. Rev. Lett. **110**, 025301 (2013).
[12] N. Murray, M. Krygier, M. Edwards, K. C. Wright, G. K. Campbell, and C. W. Clark, Probing the circulation of ring-shaped Bose-Einstein condensates, Phys. Rev. A **88**, 053615 (2013).
[13] S. Eckel, J. G. Lee, F. Jendrzejewski, N. Murray, C. W. Clark, C. J. Lobb, W. D. Phillips, M. Edwards, and G. K. Campbell, Hysteresis in a quantized superfluid 'atomtronic' circuit, Nature (London) **506**, 200 (2014).
[14] F. Jendrzejewski, S. Eckel, N. Murray, C. Lanier, M. Edwards, C. J. Lobb, and G. K. Campbell, Resistive flow in a weakly interacting Bose-Einstein condensate, Phys. Rev. Lett. **113**, 045305 (2014).
[15] Y. Guo, R. Dubessy, M. de Goër de Herve, A. Kumar, T. Badr, A. Perrin, L. Longchambon, and H. Perrin, Supersonic rotation of a superfluid: A long-lived dynamical ring, Phys. Rev. Lett. **124**, 025301 (2020).
[16] J. Polo, W. J. Chetcuti, T. Haug, A. Minguzzi, K. Wright, and L. Amico, Persistent currents in ultracold gases, arXiv:2410.17318.
[17] B. D. Josephson, Possible new effects in superconductive tunnelling, Phys. Lett. **1**, 251 (1962).
[18] A. Smerzi, S. Fantoni, S. Giovanazzi, and S. R. Shenoy, Quantum coherent atomic tunneling between two trapped Bose-Einstein condensates, Phys. Rev. Lett. **79**, 4950 (1997).
[19] I. Marino, S. Raghavan, S. Fantoni, S. R. Shenoy, and A. Smerzi, Bose-condensate tunneling dynamics: Momentum-shortened pendulum with damping, Phys. Rev. A **60**, 487 (1999).
[20] M. Albiez, R. Gati, J. Fölling, S. Hunsmann, M. Cristiani, and M. K. Oberthaler, Direct observation of tunneling and nonlinear

self-trapping in a single bosonic Josephson junction, Phys. Rev. Lett. **95**, 010402 (2005).
[21] R. Gati and M. K. Oberthaler, A bosonic Josephson junction, J. Phys. B: At. Mol. Opt. Phys. **40**, R61(R) (2007).
[22] S. Levy, E. Lahoud, I. Shomroni, and J. Steinhauer, The a.c. and d.c. Josephson effects in a Bose–Einstein condensate, Nature (London) **449**, 579 (2007).
[23] L. J. LeBlanc, A. B. Bardon, J. McKeever, M. H. T. Extavour, D. Jervis, J. H. Thywissen, F. Piazza, and A. Smerzi, Dynamics of a tunable superfluid junction, Phys. Rev. Lett. **106**, 025302 (2011).
[24] A. Gallemí, A. M. Mateo, R. Mayol, and M. Guilleumas, Coherent quantum phase slip in two-component bosonic atomtronic circuits, New J. Phys. **18**, 015003 (2015).
[25] A. Gallemí, M. Guilleumas, R. Mayol, and A. Muñoz Mateo, Multidimensional Josephson vortices in spin-orbit-coupled Bose-Einstein condensates: Snake instability and decay through vortex dipoles, Phys. Rev. A **93**, 033618 (2016).
[26] G. Spagnolli, G. Semeghini, L. Masi, G. Ferioli, A. Trenkwalder, S. Coop, M. Landini, L. Pezzè, G. Modugno, M. Inguscio, A. Smerzi, and M. Fattori, Crossing over from attractive to repulsive interactions in a tunneling bosonic Josephson junction, Phys. Rev. Lett. **118**, 230403 (2017).
[27] M. Pigneur, T. Berrada, M. Bonneau, T. Schumm, E. Demler, and J. Schmiedmayer, Relaxation to a phase-locked equilibrium state in a one-dimensional bosonic Josephson junction, Phys. Rev. Lett. **120**, 173601 (2018).
[28] I. Lesanovsky and W. von Klitzing, Spontaneous emergence of angular momentum Josephson oscillations in coupled annular Bose-Einstein condensates, Phys. Rev. Lett. **98**, 050401 (2007).
[29] J. Brand, T. J. Haigh, and U. Zülicke, Rotational fluxons of Bose-Einstein condensates in coplanar double-ring traps, Phys. Rev. A **80**, 011602 (2009).
[30] J. Brand, T. J. Haigh, and U. Zülicke, Sign of coupling in barrier-separated Bose-Einstein condensates and stability of double-ring systems, Phys. Rev. A **81**, 025602 (2010).
[31] F. Malet, G. M. Kavoulakis, and S. M. Reimann, Mixtures of Bose gases confined in concentrically coupled annular traps, Phys. Rev. A **81**, 013630 (2010).
[32] D. Aghamalyan, L. Amico, and L. C. Kwek, Effective dynamics of cold atoms flowing in two ring-shaped optical potentials with tunable tunneling, Phys. Rev. A **88**, 063627 (2013).
[33] X.-F. Zhang, B. Li, and S.-G. Zhang, Rotating spin–orbit coupled Bose–Einstein condensates in concentrically coupled annular traps, Laser Phys. **23**, 105501 (2013).
[34] S.-W. Su, S.-C. Gou, A. Bradley, O. Fialko, and J. Brand, Kibble-Zurek scaling and its breakdown for spontaneous generation of Josephson vortices in Bose-Einstein condensates, Phys. Rev. Lett. **110**, 215302 (2013).
[35] J. Polo, A. Benseny, T. Busch, V. Ahufinger, and J. Mompart, Transport of ultracold atoms between concentric traps via spatial adiabatic passage, New J. Phys. **18**, 015010 (2016).
[36] T. Bland, I. V. Yatsuta, M. Edwards, Y. O. Nikolaieva, A. O. Oliinyk, A. I. Yakimenko, and N. P. Proukakis, Persistent current oscillations in a double-ring quantum gas, Phys. Rev. Res. **4**, 043171 (2022).
[37] N. Bazhan, A. Svetlichnyi, D. Pfeiffer, D. Derr, G. Birkl, and A. Yakimenko, Generation of Josephson vortices in stacked toroidal Bose-Einstein condensates, Phys. Rev. A **106**, 043305 (2022).
[38] Y. Borysenko, N. Bazhan, O. Prykhodko, D. Pfeiffer, L. Lind, G. Birkl, and A. Yakimenko, Acceleration-driven dynamics of Josephson vortices in coplanar superfluid rings, arXiv:2411.09186.
[39] A. Chaika, A. O. Oliinyk, I. V. Yatsuta, N. P. Proukakis, M. Edwards, A. I. Yakimenko, and T. Bland, Acceleration-induced transport of quantum vortices in joined atomtronic circuits, SciPost Phys. **19**, 005 (2025).
[40] D. Roditchev, C. Brun, L. Serrier-Garcia, J. C. Cuevas, V. H. L. Bessa, M. V. Milošević, F. Debontridder, V. Stolyarov, and T. Cren, Direct observation of Josephson vortex cores, Nat. Phys. **11**, 332 (2015).
[41] D. Caputo, N. Bobrovska, D. Ballarini, M. Matuszewski, M. De Giorgi, L. Dominici, K. West, L. N. Pfeiffer, G. Gigli, and D. Sanvitto, Josephson vortices induced by phase twisting a polariton superfluid, Nat. Photon. **13**, 488 (2019).
[42] V. M. Kaurov and A. B. Kuklov, Josephson vortex between two atomic Bose-Einstein condensates, Phys. Rev. A **71**, 011601 (2005).
[43] T. W. A. Montgomery, W. Li, and T. M. Fromhold, Spin Josephson vortices in two tunnel-coupled spinor Bose gases, Phys. Rev. Lett. **111**, 105302 (2013).
[44] A. Oliinyk, B. Malomed, and A. Yakimenko, Nonlinear dynamics of Josephson vortices in merging superfluid rings, Commun. Nonlinear Sci. Numer. Simul. **83**, 105113 (2020).
[45] A. Tononi, L. Salasnich, and A. Yakimenko, Quantum vortices in curved geometries, AVS Quantum Sci. **6**, 030502 (2024).
[46] T. Lahaye, C. Menotti, L. Santos, M. Lewenstein, and T. Pfau, The physics of dipolar bosonic quantum gases, Rep. Prog. Phys. **72**, 126401 (2009).
[47] F. Böttcher, J.-N. Schmidt, J. Hertkorn, K. S. H. Ng, S. D. Graham, M. Guo, T. Langen, and T. Pfau, New states of matter with fine-tuned interactions: quantum droplets and dipolar supersolids, Rep. Prog. Phys. **84**, 012403 (2021).
[48] L. Chomaz, I. Ferrier-Barbut, F. Ferlaino, B. Laburthe-Tolra, B. L. Lev, and T. Pfau, Dipolar physics: a review of experiments with magnetic quantum gases, Rep. Prog. Phys. **86**, 026401 (2023).
[49] K. Mukherjee, T. A. Cardinale, L. Chergui, P. Sturmer, and S. M. Reimann, Droplets and supersolids in ultra-cold atomic quantum gases, Eur. Phys. J. Spec. Top. **232**, 3417 (2023),.
[50] A. Griesmaier, J. Werner, S. Hensler, J. Stuhler, and T. Pfau, Bose-Einstein condensation of chromium, Phys. Rev. Lett. **94**, 160401 (2005).
[51] J. Stuhler, A. Griesmaier, T. Koch, M. Fattori, T. Pfau, S. Giovanazzi, P. Pedri, and L. Santos, Observation of dipole-dipole interaction in a degenerate quantum gas, Phys. Rev. Lett. **95**, 150406 (2005).
[52] H.-Y. Lu, H. Lu, J.-N. Zhang, R.-Z. Qiu, H. Pu, and S. Yi, Spatial density oscillations in trapped dipolar condensates, Phys. Rev. A **82**, 023622 (2010).
[53] M. Lu, N. Q. Burdick, S. Ho Youn, and B. L. Lev, Strongly dipolar Bose-Einstein condensate of dysprosium, Phys. Rev. Lett. **107**, 190401 (2011).
[54] K. Aikawa, A. Frisch, M. Mark, S. Baier, A. Rietzler, R. Grimm, and F. Ferlaino, Bose-Einstein condensation of erbium, Phys. Rev. Lett. **108**, 210401 (2012).
[55] Y. Miyazawa, R. Inoue, H. Matsui, G. Nomura, and M. Kozuma, Bose-Einstein condensation of europium, Phys. Rev. Lett. **129**, 223401 (2022).

[56] H. Kadau, M. Schmitt, M. Wenzel, C. Wink, T. Maier, I. Ferrier-Barbut, and T. Pfau, Observing the Rosensweig instability of a quantum ferrofluid, Nature (London) **530**, 194 (2016).

[57] I. Ferrier-Barbut, H. Kadau, M. Schmitt, M. Wenzel, and T. Pfau, Observation of quantum droplets in a strongly dipolar Bose gas, Phys. Rev. Lett. **116**, 215301 (2016).

[58] F. Böttcher, J.-N. Schmidt, M. Wenzel, J. Hertkorn, M. Guo, T. Langen, and T. Pfau, Transient supersolid properties in an array of dipolar quantum droplets, Phys. Rev. X **9**, 011051 (2019).

[59] L. Tanzi, E. Lucioni, F. Famà, J. Catani, A. Fioretti, C. Gabbanini, R. N. Bisset, L. Santos, and G. Modugno, Observation of a dipolar quantum gas with metastable supersolid properties, Phys. Rev. Lett. **122**, 130405 (2019).

[60] L. Chomaz, D. Petter, P. Ilzhöfer, G. Natale, A. Trautmann, C. Politi, G. Durastante, R. M. W. van Bijnen, A. Patscheider, M. Sohmen, M. J. Mark, and F. Ferlaino, Long-lived and transient supersolid behaviors in dipolar quantum gases, Phys. Rev. X **9**, 021012 (2019).

[61] M. A. Norcia, C. Politi, L. Klaus, E. Poli, M. Sohmen, M. J. Mark, R. N. Bisset, L. Santos, and F. Ferlaino, Two-dimensional supersolidity in a dipolar quantum gas, Nature (London) **596**, 357 (2021); E. P. Gross, Classical theory of boson wave fields, Ann. Phys. **4**, 57 (1958); C. N. Yang, Concept of off-diagonal long-range order and the quantum phases of liquid He and of superconductors, Rev. Mod. Phys. **34**, 694 (1962); G. V. Chester, Speculations on Bose-Einstein condensation and quantum crystals, Phys. Rev. A **2**, 256 (1970); A. J. Leggett, Can a solid be "superfluid"? Phys. Rev. Lett. **25**, 1543 (1970).

[62] M. Boninsegni and N. V. Prokof'ev, *Colloquium:* Supersolids: What and where are they? Rev. Mod. Phys. **84**, 759 (2012).

[63] M. Guo, F. Böttcher, J. Hertkorn, J.-N. Schmidt, M. Wenzel, H. P. Büchler, T. Langen, and T. Pfau, The low-energy Goldstone mode in a trapped dipolar supersolid, Nature (London) **574**, 386 (2019); G. Natale, R. M. W. van Bijnen, A. Patscheider, D. Petter, M. J. Mark, L. Chomaz, and F. Ferlaino, Excitation spectrum of a trapped dipolar supersolid and its experimental evidence, Phys. Rev. Lett. **123**, 050402 (2019); J. Hertkorn, F. Böttcher, M. Guo, J. N. Schmidt, T. Langen, H. P. Büchler, and T. Pfau, Fate of the amplitude mode in a trapped dipolar supersolid, *ibid.* **123**, 193002 (2019); J.-N. Schmidt, J. Hertkorn, M. Guo, F. Böttcher, M. Schmidt, K. S. H. Ng, S. D. Graham, T. Langen, M. Zwierlein, and T. Pfau, Roton excitations in an oblate dipolar quantum gas, *ibid.* **126**, 193002 (2021); J. Hertkorn, J.-N. Schmidt, M. Guo, F. Böttcher, K. S. H. Ng, S. D. Graham, P. Uerlings, H. P. Büchler, T. Langen, M. Zwierlein, and T. Pfau, Supersolidity in two-dimensional trapped dipolar droplet arrays, *ibid.* **127**, 155301 (2021); J. Hertkorn, J.-N. Schmidt, F. Böttcher, M. Guo, M. Schmidt, K. S. H. Ng, S. D. Graham, H. P. Büchler, T. Langen, M. Zwierlein, and T. Pfau, Density fluctuations across the superfluid-supersolid phase transition in a dipolar quantum gas, Phys. Rev. X **11**, 011037 (2021).

[64] C. Bühler, T. Ilg, and H. P. Büchler, Quantum fluctuations in one-dimensional supersolids, Phys. Rev. Res. **5**, 033092 (2023). E. Poli, D. Baillie, F. Ferlaino, and P. B. Blakie, Excitations of a two-dimensional supersolid, Phys. Rev. A **110**, 053301 (2024).

[65] L. Tanzi, S. M. Roccuzzo, E. Lucioni, F. Fama, A. Fioretti, C. Gabbanini, G. Modugno, A. Recati, and S. Stringari, Supersolid symmetry breaking from compressional oscillations in a dipolar quantum gas, Nature (London) **574**, 382 (2019); P. Ilzhöfer, M. Sohmen, G. Durastante, C. Politi, A. Trautmann, G. Natale, G. Morpurgo, T. Giamarchi, L. Chomaz, M. J. Mark, and F. Ferlaino, Phase coherence in out-of-equilibrium supersolid states of ultracold dipolar atoms, Nat. Phys. **17**, 356 (2021); M. Sohmen, C. Politi, L. Klaus, L. Chomaz, M. J. Mark, M. A. Norcia, and F. Ferlaino, Birth, life, and death of a dipolar supersolid, Phys. Rev. Lett. **126**, 233401 (2021); T. Bland, E. Poli, C. Politi, L. Klaus, M. A. Norcia, F. Ferlaino, L. Santos, and R. N. Bisset, Two-dimensional supersolid formation in dipolar condensates, *ibid.* **128**, 195302 (2022); A. Alaña, Iñigo L. Egusquiza, and M. Modugno, Supersolid formation in a dipolar condensate by roton instability, Phys. Rev. A **108**, 033316 (2023); K. Mukherjee and S. M. Reimann, Classical-linear-chain behavior from dipolar droplets to supersolids, *ibid.* **107**, 043319 (2023); S. I. Mistakidis, K. Mukherjee, S. M. Reimann, and H. R. Sadeghpour, Tunneling dynamics of ^{164}Dy supersolids and droplets, *ibid.* **110**, 013323 (2024).

[66] S. M. Roccuzzo, A. Gallemí, A. Recati, and S. Stringari, Rotating a supersolid dipolar gas, Phys. Rev. Lett. **124**, 045702 (2020).

[67] A. Gallemí, S. M. Roccuzzo, S. Stringari, and A. Recati, Quantized vortices in dipolar supersolid Bose-Einstein-condensed gases, Phys. Rev. A **102**, 023322 (2020).

[68] M. Šindik, A. Recati, S. M. Roccuzzo, L. Santos, and S. Stringari, Creation and robustness of quantized vortices in a dipolar supersolid when crossing the superfluid-to-supersolid transition, Phys. Rev. A **106**, L061303 (2022).

[69] L. Klaus, T. Bland, E. Poli, C. Politi, G. Lamporesi, E. Casotti, R. N. Bisset, M. J. Mark, and F. Ferlaino, Observation of vortices and vortex stripes in a dipolar condensate, Nat. Phys. **18**, 1453 (2022).

[70] E. Casotti, E. Poli, L. Klaus, A. Litvinov, C. Ulm, C. Politi, M. J. Mark, T. Bland, and F. Ferlaino, Observation of vortices in a dipolar supersolid, Nature (London) **635**, 327 (2024).

[71] M. Abad, M. Guilleumas, R. Mayol, M. Pi, and D. M. Jezek, A dipolar self-induced bosonic Josephson junction, Europhys. Lett. **94**, 10004 (2011).

[72] G. Biagioni, N. Antolini, B. Donelli, L. Pezzè, A. Smerzi, M. Fattori, A. Fioretti, C. Gabbanini, M. Inguscio, L. Tanzi, and G. Modugno, Measurement of the superfluid fraction of a supersolid by Josephson effect, Nature (London) **629**, 773 (2024).

[73] L. M. Platt, D. Baillie, and P. B. Blakie, Supersolid spectroscopy, Phys. Rev. A **111**, 053305 (2025).

[74] B. Donelli, N. Antolini, G. Biagioni, M. Fattori, A. Fioretti, C. Gabbanini, M. Inguscio, L. Tanzi, G. Modugno, A. Smerzi, and L. Pezzè, Self-induced Josephson oscillations and self-trapping in a supersolid dipolar quantum gas, arXiv:2501.17142.

[75] A. Alaña, M. Modugno, P. Capuzzi, and D. M. Jezek, Self-sustained Josephson dynamics and self-trapping in supersolids, arXiv:2501.08739.

[76] M. Nilsson Tengstrand, D. Boholm, R. Sachdeva, J. Bengtsson, and S. M. Reimann, Persistent currents in toroidal dipolar supersolids, Phys. Rev. A **103**, 013313 (2021).

[77] M. Nilsson Tengstrand, P. Stürmer, J. Ribbing, and S. M. Reimann, Toroidal dipolar supersolid with a rotating weak link, Phys. Rev. A **107**, 063316 (2023).

[78] M. Šindik, T. Zawiślak, A. Recati, and S. Stringari, Sound, superfluidity, and layer compressibility in a ring dipolar supersolid, Phys. Rev. Lett. **132**, 146001 (2024).

[79] J. Hertkorn, P. Stürmer, K. Mukherjee, K. S. H. Ng, P. Uerlings, F. Hellstern, L. Lavoine, S. M. Reimann, T. Pfau, and R. Klemt, Decoupled sound and amplitude modes in trapped dipolar supersolids, Phys. Rev. Res. **6**, L042056 (2024).

[80] A. R. P. Lima and A. Pelster, Quantum fluctuations in dipolar Bose gases, Phys. Rev. A **84**, 041604 (2011).

[81] A. R. P. Lima and A. Pelster, Beyond mean-field low-lying excitations of dipolar Bose gases, Phys. Rev. A **86**, 063609 (2012).

[82] B. Mottelson, Yrast spectra of weakly interacting Bose-Einstein condensates, Phys. Rev. Lett. **83**, 2695 (1999).

[83] M. J. A. de Voigt, J. Dudek, and Z. Szymański, High-spin phenomena in atomic nuclei, Rev. Mod. Phys. **55**, 949 (1983).

[84] S. Komineas, N. R. Cooper, and N. Papanicolaou, Single vortex states in a confined Bose-Einstein condensate, Phys. Rev. A **72**, 053624 (2005).

[85] K. Kärkkäinen, J. Christensson, G. Reinisch, G. M. Kavoulakis, and S. M. Reimann, Metastability of persistent currents in trapped gases of atoms, Phys. Rev. A **76**, 043627 (2007).

[86] A. J. Leggett, On the superfluid fraction of an arbitrary many-body system at $T = 0$, J. Stat. Phys. **93**, 927 (1998).

[87] J. Sánchez-Baena, C. Politi, F. Maucher, F. Ferlaino, and T. Pohl, Heating a quantum dipolar fluid into a solid, Nat. Commun. **14**, 1868 (2022).

[88] W. Bao, D. Jaksch, and P. A. Markowich, Numerical solution of the Gross–Pitaevskii equation for Bose–Einstein condensation, J. Comput. Phys. **187**, 318 (2003).

[89] W. Bao, S. Jin, and P. A. Markowich, Numerical study of time-splitting spectral discretizations of nonlinear Schrödinger equations in the semiclassical regimes, SIAM J. Sci. Comput. **25**, 27 (2003).